Ergodicity and Born's rule in an entangled three-qubit Bohmian system

Athanasios C. Tzemos [*] and George Contopoulos[†]

Research Center for Astronomy and Applied Mathematics, Academy of Athens, Soranou Efesiou 4, Athens GR-11527, Greece

We study in detail the interplay between chaos and entanglement in the Bohmian trajectories of three entangled qubits, made of coherent states of the quantum harmonic oscillator. We find that all the three-dimensional (3D) chaotic trajectories are ergodic; namely, they have a common long time distribution of points regardless of the initial conditions, and for any nonzero entanglement, their number is much larger than in the corresponding two-qubit system. Furthermore, the range of entanglements for which practically all the trajectories are chaotic and ergodic is much larger than in the two-qubit case. Thus, as the dimensionality of the system increases, Born's rule becomes accessible to a wider range of arbitrary initial distributions than in the 2D case. Our numerical results lead to the conjecture that, for multiqubit systems, Born's rule is the limit of almost all initial distributions of particles.

I. INTRODUCTION

According to Born's rule (BR), the probability density of finding a quantum particle in a region of space is given by the squared absolute value of its wave function Φ, i.e., $P = |\Phi|^2$. Born's rule is a key postulate of standard quantum mechanics and has never been doubted by the experiment.

In Bohmian quantum mechanics (BQM) [1–3], where the quantum particles are guided by the wave function Φ [4–7] according to the so-called Bohmian equations of motion

$$m_i \frac{dx_i}{dt} = \hbar Im\left(\frac{\nabla_i \Phi}{\Phi}\right), \tag{1}$$

we are, in principle, allowed to consider an initial distribution of particles with probability density $P_0 \neq |\Phi_0|^2$. Consequently, it is of fundamental importance in BQM to understand the mechanism that leads an arbitrary particle distribution to that dictated by BR. The origin of BR in the Bohmian framework has been studied extensively in the past [8–17], but it remains a point of contention.

The nonlinear character of Bohmian equations implies that for a generic Bohmian system ordered and chaotic trajectories coexist.[1] Thus, the BR distribution of a Bohmian system contains, in principle, both ordered and chaotic trajectories. However, the behavior of ordered trajectories is very different to that of the chaotic ones. Consequently it is crucial to understand the role of both kinds of Bohmian trajectories and their contribution in a large collective distribution of Bohmian particles. The generation of chaos in BQM has been studied by many authors in the past. In particular, Frisk [18], Bialynicki-

Birula *et al.* [19], Falsaperla and Fonte [20], Sanz *et al.* [21], Wisniacki and Pujals [22], Wisniacki *et al.* [23,24], Borondo *et al.* [25], and Efthymiopoulos and Contopoulos [26] have shown the key role of the nodal points (the points where the wave function vanishes) for the generation of chaotic Bohmian trajectories.

In Refs. [27,28] we presented a general theoretical mechanism for the generation of chaos in arbitrary two-dimensional (2D) and 3D Bohmian systems. This was the so-called "nodal point–X-point complex mechanism," according to which, whenever a quantum particle comes close to a nodal point of the wave function, it gets scattered by a nearby characteristic stagnant point of the Bohmian flow in the frame of reference of the moving node, the so-called X-point. The cumulative action of many such scattering events implies the saturation of the Lyapunov characteristic number at a positive value, something that indicates the existence of chaos. Nodal points along with their corresponding X-points form a characteristic structure of the Bohmian flow, called the "nodal point–X-point complex" (NPXPC).

In our latest series of works [29–32] we focused on the application of the NPXPC mechanism in an entangled bipartite qubit system made of coherent states of the quantum harmonic oscillator. This system, besides its theoretical and experimental significance in quantum information theory and quantum optics [33–37], has also many interesting characteristics and advantages from a Bohmian perspective.

(i) Its probability density has two distinct Gaussian blobs whose geometrical characteristics and motions in time can be easily studied.

(ii) It has infinitely many NPXPCs lying on straight lattices, whose positions can be analytically found, something that facilitates significantly the computations.

(iii) It is in direct correspondence with a two-spin-qubit system. In fact its entanglement [38–40] can be easily manipulated by only one parameter and spans from zero entanglement (product state) to maximum entanglement (Bell state) [33].

---

*atzemos@academyofathens.gr

†gcontop@academyofathens.gr

[1]By saying chaotic trajectories we mean trajectories with high sensitivity to initial conditions, as in the case of classical dynamical systems.

054211-1

Besides the evolution of the trajectories of this system, we also considered the role of chaos and order in establishing Born's rule ($P = |\Phi|^2$). We found that when the entanglement is large most trajectories are chaotic and in the long run the form of the distribution of their points approaches that of Born's distribution.

In fact the chaotic trajectories of this system were found to be ergodic, since their points cover densely the support of the wave function[2] and tend to the same final distribution regardless of the initial conditions (for a study of ergodicity in BQM, see also Refs. [41,42]). This distribution is different in general from the BR distribution, due to the existence of the ordered trajectories. This difference becomes larger with the decrease of the entanglement due to the significant number of ordered trajectories in the weakly entangled states. Consequently, ergodicity is not sufficient to guarantee the establishment of BR for any initial distribution, but only for those distributions with a ratio between ordered and chaotic trajectories equal approximately to the corresponding ratio of the BR distribution [32].

In the present paper we extend our previous calculations by adding another qubit in the third direction. The transition from two to three dimensions implies many technical difficulties in the calculations of the Bohmian trajectories and large computational times for the numerical simulations. That is why only a few works have been published in 3D Bohmian systems [18,20,28,43,44] and no one with references to multiparticle distributions and Born's rule. In fact, the infinitely long straight lattices of NPXPCs of the 2D case become infinitely long 2D grids of NPXPCs embedded in the 3D space, which wander around the configuration space and scatter the approaching trajectories in a very complex way. However, we managed to calculate analytically the positions of these grids in space and time.

We consider a wave function which is a superposition of two individual solutions of the unperturbed 3D quantum harmonic oscillator and covers all the range from zero entanglement up to maximum tripartite entanglement [38,45].

We find first that the chaotic trajectories are ergodic, i.e., the limiting distribution of their points is the same regardless of their initial conditions, just as in the two-qubit case. For strongly entangled states we find that all (or the vast majority) of the Bohmian trajectories are chaotic and the pattern of their limiting distributions is the same (or approximately the same) as that of Born's rule, while in the opposite extreme case of zero entanglement, all the trajectories are ordered and they form 3D Lissajous figures; i.e., they fill rectangular 3D boxes (just as the 2D Lissajous figures in the two-qubit case). In this case BR is not accessible by initial distributions with $P_0 \neq |\Phi_0|^2$.

However, the increase of the number of the qubits implies drastic changes in the intermediate and weakly entangled states, where chaotic and ordered trajectories coexist. We find that as the dimensionality increases from 2 to 3, there are more

chaotic trajectories for any nonzero amount of entanglement than in the 2D case. Moreover, the chaotic trajectories are ergodic in all cases, but for weak entanglements the ergodic character of the chaotic trajectories is established after a longer time.

Based on our results in two and three dimensions, we expect that the increase of the chaotic trajectories will become even stronger with further increase of the degrees of freedom, so that in the case of multiqubit systems almost all initial particle distributions will tend to BR.

The present paper is organized as follows: In Sec. II we describe our wave function and the form of its support in the configuration space. Then in Sec. III we present the form of the 3D NPXPCs and the analytical formulas of their position in space as a function of time (the detailed calculation is presented in the Appendix). In Sec. IV we find the distribution of the points of the chaotic trajectories for various amounts of the entanglement and show that they tend to the same limiting distribution. The form of these distributions is different from that of the corresponding Born's distribution and this difference becomes larger as the entanglement decreases. In Sec. V we calculate the ratio between the ordered and the chaotic trajectories inside the BR distribution for various amounts of entanglement and emphasize its difference with that of the corresponding two-qubit case. Finally, in Sec. VI we summarize the similarities and the differences between the two-qubit and the three-qubit cases and draw our final conclusions.

II. TIME EVOLUTION OF THE WAVE FUNCTION

We extend our previous studies [29–32] to the case of a 3D wave function,

$$\Phi = c_1 Y_R(x, t) Y_R(y, t) Y_R(z, t) + c_2 Y_L(x, t) Y_L(y, t) Y_L(z, t), \tag{2}$$

where

$$
\begin{aligned}
Y_{R/L}&(q, t) \\
&= \left(\frac{\omega_q}{\pi}\right)^{\frac{1}{4}} \exp\left[-\frac{\omega_q}{2}\left(i \mp \sqrt{\frac{2}{\omega_q}} a_0 \cos(\omega_q t)\right)^2 \right. \\
&\quad \left. + i\left(\mp\sqrt{2\omega_q} a_0 q \sin(\omega_q t) + \frac{a_0^2 \sin(2\omega_q t) - \omega_q t}{2}\right)\right],
\end{aligned}
\tag{3}
$$

and $q = x$, y, or z. Furthermore c_1 and c_2 are real coefficients and $c_1^2 + c_2^2 = 1$. $Y_{R/L}$ refers to a coherent state which for $t = 0$ is on the right or left from the center of the oscillation. Similarly to the 2D case, the entanglement of the state Φ in Eq. (2) can be controlled by the coefficient c_2, by working in the range $[0, \sqrt{2}/2]$. For $c_2 = 0$ we have a product state (nonentangled state) and for $c_2 = \sqrt{2}/2$ we have a maximally entangled three-qubit state, the so-called Greenberger-Horne-Zeilinger (GHZ) state [33].[3]

---

[2]The support is the region of the configuration space where the probability density of the wave function has appreciable value. In the present work we consider as support the region of the configuration space with probability density larger than 5×10^{-4}.

---

[3]The quantification of multipartite entanglement remains an open problem in quantum information theory [45].
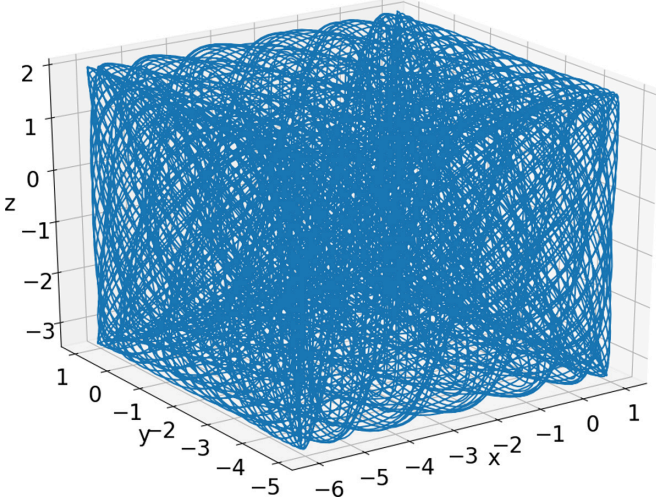
FIG. 1. The ordered trajectory of a particle with ($x_0 = 1$, $y_0 = 1$, and $z_0 = 2$) in the case $c_2 = 0$ (product state) for $t \in [0, 1000]$. It is a 3D Lissajous figure.

We further assume that the frequencies have an incommensurable ratio. In our calculations we worked with $\omega_x = 1$, $\omega_y = \sqrt{2}$, $\omega_z = \sqrt{3}$, and $a_0 = 2.5$.

Regarding the probability density $|\Phi|^2$, in the product case $c_2 = 0$ ($c_1 = 1$) we have a 4D blob, called hereafter "hyperblob," around a point with

$$x_c = \sqrt{\frac{2}{\omega_x}} a_0 \cos(\omega_x t), \quad y_c = \sqrt{\frac{2}{\omega_y}} a_0 \cos(\omega_y t),$$

$$z_c = \sqrt{\frac{2}{\omega_z}} a_0 \cos(\omega_z t). \tag{4}$$

Consequently the center (x_c, y_c, z_c) of the hyperblob, which for our numerical values starts at $x_c = 3.54$, $y_c = 2.97$, and $z_c = 2.69$, forms a 3D Lissajous curve with corresponding periods $T_x = 2\pi/\omega_x = 2\pi$, $T_y = 2\pi/\omega_y \simeq 4.44$, and $T_z = 2\pi/\omega_z \simeq 3.63$. The corresponding value of Φ is

$$\Phi_c = \left(\frac{\omega_x \omega_y \omega_z}{\pi^3}\right)^{\frac{1}{4}} \exp\left\{-\frac{i}{2}\left[a_0^2[\sin(2\omega_x t) + \sin(2\omega_y t)\right.\right.$$

$$\left.\left. + \sin(2\omega_z t)] + (\omega_x + \omega_y + \omega_z)t\right]\right\} \tag{5}$$

and the center (x_c, y_c, z_c) is always at the maximum of the corresponding $|\Phi|^2$, equal to $|\Phi_{\max}|^2 = (\frac{\omega_x \omega_y \omega_z}{\pi^3})^{\frac{1}{2}} \simeq 0.28$. All the Bohmian trajectories in this case follow the Lissajous

figure of the hyperblob, filling a rectangular box, like the one shown in Fig. 1.

Similarly, in the case $c_1 = 0$ ($c_2 = 1$) we have a blob around the symmetric point $x_c' = -x_c$, $y_c' = -y_c$, and $z_c' = -z_c$. When $c_1 c_2 \neq 0$ both hyperblobs coexist, while their sizes depend on the amount of the entanglement. If we set the values (4) in Eq. (2) we find

$$\Phi = c_1 \Phi_c + c_2 \left(\frac{\omega_x \omega_y \omega_z}{\pi^3}\right)^{\frac{1}{2}} \exp\left(-4a_0^2[\cos^2(\omega_x t)\right.$$

$$+ \cos^2(\omega_y t) + \cos^2(\omega_z t)]$$

$$+ \frac{i}{2}\left\{3a_0^2[\sin(2\omega_x t) + \sin(2\omega_y t) + \sin(2\omega_z t)]\right.$$

$$\left.\left. - (\omega_x + \omega_y + \omega_z)t\right\}\right). \tag{6}$$

Therefore the second exponential is not only an imaginary quantity as in Eq. (5) but it has also a very small, in general, real factor of the form $E = \exp\{-25[\cos^2 t + \cos^2(\sqrt{2}t) + \cos^2(\sqrt{3}t)]\}$. Thus, only when the quantity $[\cos^2 t + \cos^2(\sqrt{2}t) + \cos^2(\sqrt{3}t)]$ is very small, the term E may become of order $O(1)$ and the value of Φ is not close to $c_1 \Phi_c$. This happens when the two hyperblobs are close to collision, where all the quantities x_c, y_c, and z_c are close to zero.

In Fig. 2 we give the evolution of the hyperblobs in two cases when $c_1 = c_2 = \sqrt{2}/2$ [Fig. 2(a)] and when $c_2 = 0.2$ [Fig. 2(b)]. These figures give the forms of the isosurfaces with $|\Phi|^2 = 0.008$ for $t = 0$ [Figs. 2(a) and 2(b) (yellow)], for $t = 8$ during a collision [Figs. 2(a) and 2(b) (green)], and for $t = 11$ after the collision [Figs. 2(a) and 2(b) (blue)]. Consequently the hyperblobs are reformed after the collisions, similarly to the 2D case [30,32].

III. NODAL LINES

The nodal lines are defined by the equations

$$\Phi_{\text{real}} = \Phi_{\text{Imag}} = 0. \tag{7}$$

In the 2D case Eqs. (7) define a set of infinite nodal points lying on a straight line [Eqs. (14) of Ref. [32]]. When the two blobs collide, close to the origin, they split into a number of secondary blobs (due to their interference) that appear between the nodal points. On the other hand, when the two blobs are far from the origin, there are again extremely small blobs between the nodal points that can be considered completely insignificant.

In the present case (3D) instead of nodal points we have infinitely long nodal lines (Fig. 3). These are given by the equations

$$x_{\text{nod}}(z, t) = \frac{k\pi \cos(\omega_y t) + \sin(\omega_y t) \ln\left(\left|\frac{c_1}{c_2}\right|\right) - 2\sqrt{2\omega_z} a_0 z \sin(\omega_{zy} t)}{2\sqrt{2\omega_x} a_0 \sin(\omega_{xy} t)}, \tag{8}$$

$$y_{\text{nod}}(z, t) = -\frac{k\pi \cos(\omega_x t) + \sin(\omega_x t) \ln\left(\left|\frac{c_1}{c_2}\right|\right) - 2\sqrt{2\omega_z} a_0 z \sin(\omega_{zx} t)}{2\sqrt{2\omega_y} a_0 \sin(\omega_{xy} t)}, \tag{9}$$

where $\omega_{xy} = \omega_x - \omega_y$, $\omega_{zy} = \omega_z - \omega_y$, and $\omega_{zx} = \omega_z - \omega_x$, and k is odd for $c_1 \cdot c_2 > 0$ and even or zero for $c_1 \cdot c_2 < 0$.

For any given z the nodal lines give nodal points along straight lines, while for $z = 0$ we recover the nodal
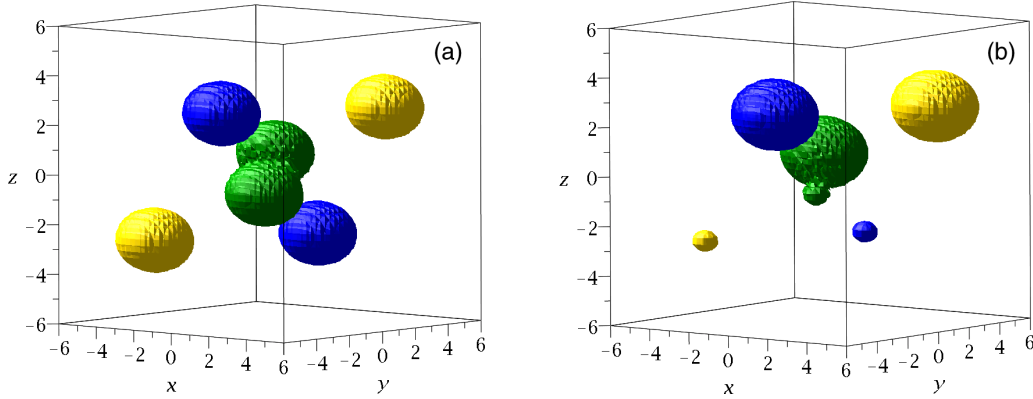
FIG. 2. The 3D isosurfaces of the 4D probability density $|\Phi|^2$ when $|\Phi|^2 = 0.008$, at $t = 0$ (yellow balls), $t = 8$ (green balls), and $t = 11$ (blue balls) for (a) $c_2 = \sqrt{2}/2$ (maximally entangled state) and (b) $c_2 = 0.2$ (weakly entangled state).

points of the corresponding 2D case $\Phi = c_1 Y_R(x, t) Y_R(y, t) + c_2 Y_L(x, t) Y_L(y, t)$. The relative distances between successive nodal points for constant z are

$$\Delta x = \frac{\pi \cos(\omega_y t)}{\sqrt{2}\omega_x a_0 \sin(\omega_{xy} t)}, \quad \Delta y = -\frac{\pi \cos(\omega_x t)}{\sqrt{2}\omega_y a_0 \sin(\omega_{xy} t)}, \tag{10}$$

and they do not depend on k, z, or c_1/c_2. The straight lines for every z are parallel with inclination $\frac{\Delta y}{\Delta x} = -\sqrt{\frac{\omega_x}{\omega_y}} \frac{\cos(\omega_x t)}{\cos(\omega_y t)}$. The nodal lines lie on a plane which rotates clockwise and counterclockwise in time. The distances between the nodal points for any z change also with time. In particular, when $t = \frac{\Lambda \pi}{\omega_{xy}}$ ($\Lambda = 0, 1, 2, \dots$) all the nodal points go to infinity.

The distance of the straight lines from the z axis ($x = y = 0$) is equal to

$$d = \frac{\ln\left(\left|\frac{c_1}{c_2}\right|\right)}{2\sqrt{2}a_0\sqrt{\omega_x \cos^2(\omega_x t) + \omega_y \cos^2(\omega_y t)}}, \tag{11}$$

which is larger than

$$d_{\min} = \ln\left(\left|\frac{c_1}{c_2}\right|\right) / (2\sqrt{2}a_0\sqrt{\omega_x + \omega_y}) \simeq 0.086 \ln\left(\left|\frac{c_1}{c_2}\right|\right). \tag{12}$$

This distance is independent of z and is the same as in the 2D case [32]. On the other hand, the distance of a nodal line [given by Eqs. (11) and (12)] from the origin is found by taking the minimum value of $r = \sqrt{x_{\text{nod}}^2 + y_{\text{nod}}^2 + z_{\text{nod}}^2}$, and this is

$$r_{\min} = \frac{\sqrt{\frac{\omega_x\left[k\pi \cos(\omega_x t) + \ln\left(\left|\frac{c_1}{c_2}\right|\right)\right]^2 + \omega_y\left[k\pi \cos(\omega_y t) + \ln\left(\left|\frac{c_1}{c_2}\right|\right)\right]^2 + \omega_z\left[k\pi \cos(\omega_z t) + \ln\left(\left|\frac{c_1}{c_2}\right|\right)\right]^2}{\omega_x\omega_y \sin^2(\omega_{xy} t) + \omega_z\omega_x \sin^2(\omega_{zx} t) + \omega_z\omega_y \sin^2(\omega_{zy} t)}}}{2\sqrt{2}a_0}. \tag{13}$$

According to the NPXPC mechanism, close to the nodal lines are the so-called X-lines, whose points are stationary with respect to the corresponding nodal points and scatter the incoming trajectories, thus leading to chaos production [27,28].

IV. TRAJECTORIES AND DISTRIBUTIONS

In order to study the Bohmian trajectories of single particle or multiparticle distributions for very long times, it is useful to construct a 3D grid covering the support of the wave function $|\Phi|^2$ and count the number of passages of the trajectories in every cell of the grid. Then we can make color plots of these countings, similarly to our figures of the 2D case, and gain significant information about the long time behavior of the trajectories.

In particular, if $S = [x(t_i), y(t_i), z(t_i)]$, with $t_i = i\Delta t$, $i = 0, 1, 2, \dots, N$, is a sample of the points of a single tra-

jectory collected with a time step Δt up to $t = t_i$, then we define the "single trajectory distribution" $P_s(x_j, y_k, z_l; t_i)$ over a grid of cubic cells around the points $(x_j, y_k, z_l) = (j\Delta x, k\Delta_y, l\Delta z)$, with $j, k, l = -N, -N+1, \dots, N-1, N$, where $N = |x_{\max}/\Delta x| = |y_{\max}/\Delta y| = |z_{\max}/\Delta z|$, as

$$P_s(x_j, y_k, z_l; t_i) = \Delta N(x_j, y_k, z_l; t_i), \tag{14}$$

where ΔN is the number of points of the sample S located within the cell defined by $x_j - \Delta x/2 \leqslant x < x_j + \Delta x/2$, $y_k - \Delta y/2 \leqslant y < y_k + \Delta y/2$, and $x_l - \Delta z/2 \leqslant z < x_l + \Delta z/2$. Consequently $\Delta N(x_j, y_k, z_l; t_i)$ is the "single trajectory occupation number" of the cell (x_j, y_k, z_l) from $t = 0$ up to $t = t_i$. Thus $P_s(x_j, y_k, z_l; t_i)$ can be represented by a $(2N + 1) \times (2N + 1) \times (2N + 1)$ matrix defined by $P_S(J, K, L) = P_S(x_{J-N-1}, y_{K-N-1}, z_{L-N-1})$, where $J, K, L = 1, 2, \dots 2N + 1$.
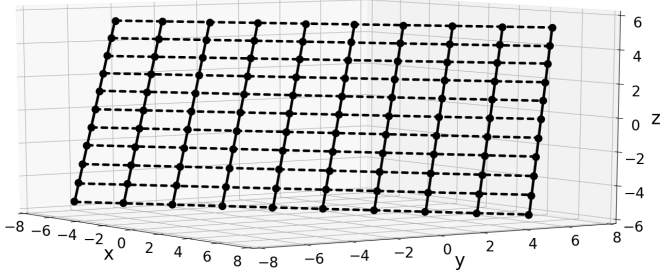
FIG. 3. Nodal lines (continuous curves along the different values of z) and nodal points (joined by dashed lines for every given value of z) for integer values of z from -5 up to 5 at time $t = 9$ for the GHZ state with k being odd in $[-9, 9]$.

We now extend the above considerations in the case of an ensemble of the points of N_P Bohmian trajectories evolved up to $t = t_i$. We define the "multiparticle distribution" as

$$P_M(x_j, y_k, z_l; t_i) = \Delta M(x_j, y_k, z_l; t_i), \quad (15)$$

$$\Delta M(x_j, y_k, z_l; t_i) = \sum_{m=1}^{N_p} \Delta N^{(m)}(x_j, y_k, z_l; t_i), \quad (16)$$

where $\Delta M(x_j, y_k, z_l; t_i)$ is the sum of the occupation numbers of the N_p trajectories and is called "multiparticle occupation number" from $t = 0$ up to $t = t_i$. Thus the multiparticle distribution can also be represented by a $(2N + 1) \times (2N + 1) \times$

$(2N + 1)$ matrix, $P_M(J, K, L) = (x_{J-N-1}, y_{K-N-1}, z_{L-N-1})$, where $J, K, L = 1, 2, \ldots 2N + 1$.

In Figs. 4(a) and 4(b) we make a 3D cubic grid and count the occupation numbers of its bins (cubic cells of side length $\simeq 0.167$) by the points of the trajectories. Our grid contains 72^3 bins from -6 to 6 in x, y, and z directions. Outside this cube, the value of $|\Phi|^2$ is, in general, smaller than 5×10^{-4} (while the maximum value of $|\Phi|^2$ is close to 0.3), and thus we cover essentially all the support of $|\Phi|^2$. The occupation number of every bin is represented by a color of the spectral color bar on the right of every figure, where for a higher number of counts we have a warmer color (towards the red). The use of a variable transparency for the points (the so-called "α channel"), which increases with the decrease of the counts in the bin, provides us a way to observe the inner structure of the 3D color map, without loss of information about the outer limits of the pattern.

In the case of the maximally entangled state, the long time distribution of the points of a single trajectory takes a characteristic form [Fig. 4(a)] that has eight regions of high concentration (red) joined by yellow lines, while outwards, beyond the red regions, the density decreases practically to zero. The sampling time of the points of the trajectories is taken to be equal to $\Delta t = 0.05$,[4] while the overall time is $t = 10^6$.

---

[4]We have checked that smaller Δt gives very similar final results.
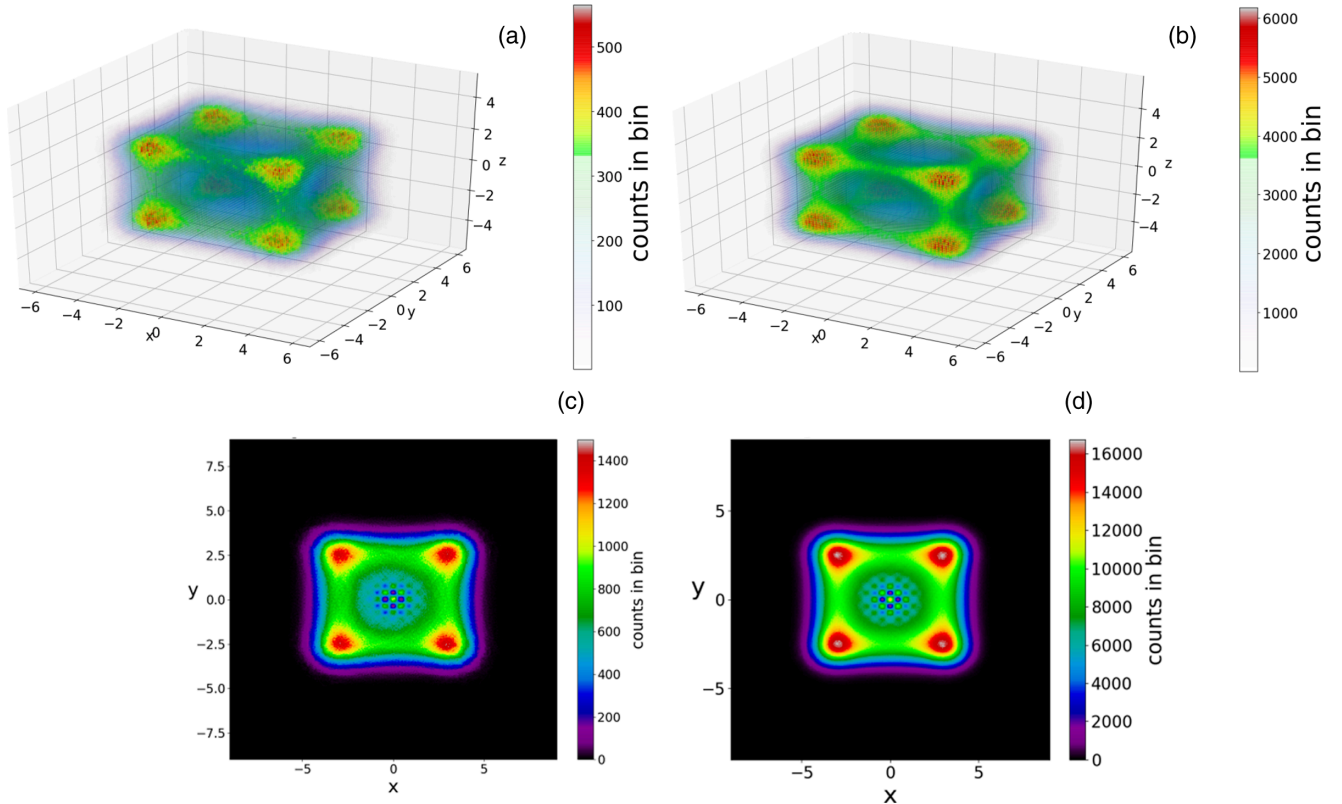
FIG. 4. The distribution of the points (a) of a single trajectory of the 3D state $c_2 = \sqrt{2}/2$ with $x_0 = 3$, $y_0 = 0$, and $z_0 = 0$ up to $t = 10^6$ and (b) of 2400 trajectories following Born's rule up to $t = 5000$. (c, d) The single-particle distribution with $x_0 = 3$ and $y_0 = 0$ and the Born distribution in the 2D state $\Phi_{2d} = c_1 Y_R(x) Y_R(y) + c_2 Y_L(x) Y_L(y)$ with $c_1 = c_2 = \sqrt{2}/2$.
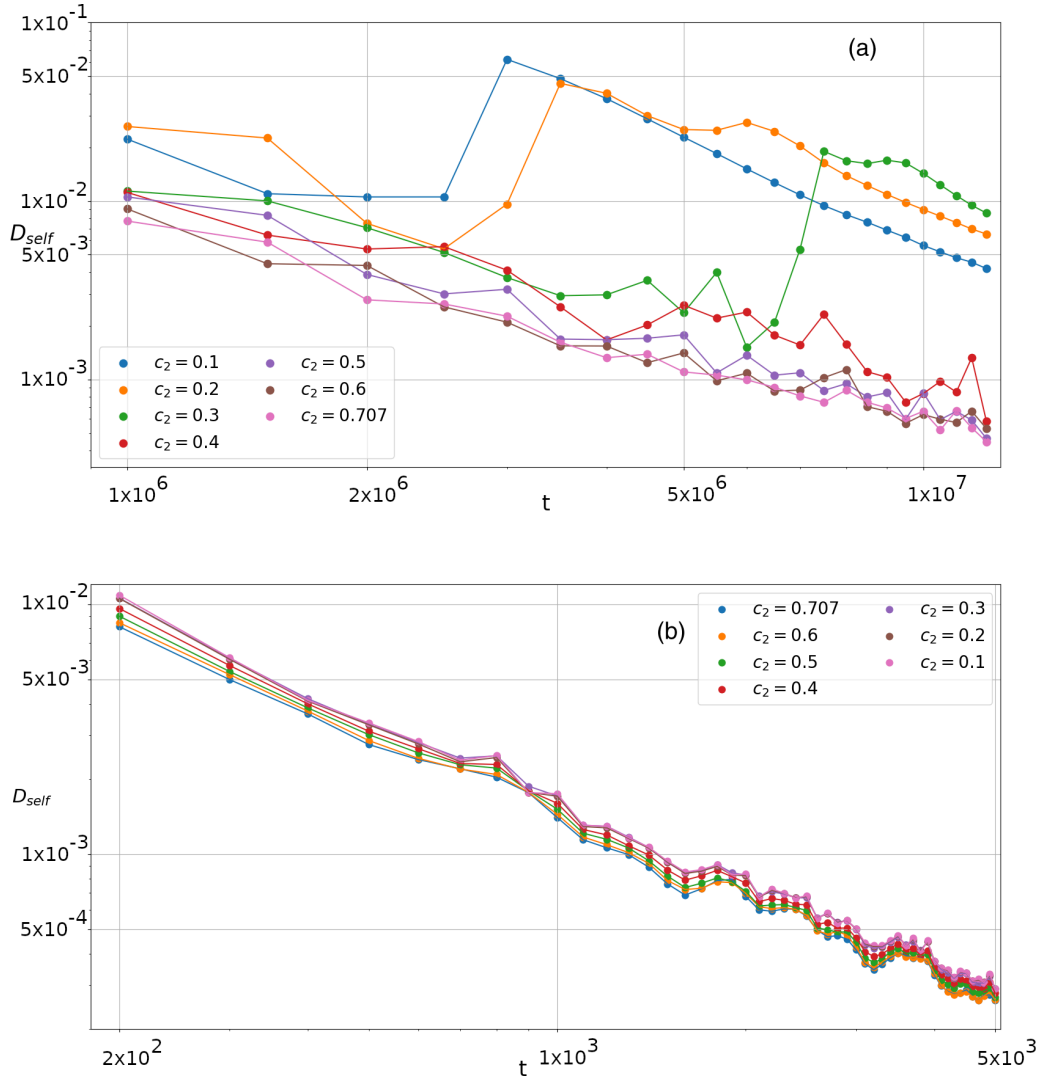
FIG. 5. The Frobenius distances between successive patterns of the points of (a) particular trajectories of various c_2 up to $t = 1.2 \times 10^7$ and (b) Born distributions containing 2400 particles for various entanglements up to $t = 5000$. In all cases the long limit variations of the self-distance of the patterns in the double logarithmic scale follow straight lines with inclinations $\simeq -1.05$.

In Fig. 4(b) we show the Born distribution of 2400 particles up to $t = 5000$. The two patterns [Fig. 4(a) and Fig. 4(b)] look very similar. In fact they are the 3D analogs of the distribution of the 2D state $\Phi_{2D} = c_1 Y_R(x) Y_R(y) + c_2 Y_L(x) Y_L(y)$ [Fig. 4(c) for a single trajectory up to $t = 10^6$ and Fig. 4(d) for 2400 trajectories up to $t = 5000$], where we have four red regions joined by yellow lines.

In the case of the GHZ state (maximum entanglement) all the trajectories are chaotic and ergodic, as in the Bell state of the 2D case. Namely, the distributions of the points of individual chaotic trajectories with the same entanglement are practically the same, and if we took individual trajectories for longer times in order to have about the same total number of points as in the case of 2400 particles satisfying the Born distribution, we would find final patterns very similar to those in Fig. 4(a). In fact, the number of points in the second case is $20 \times 5000 \times 2400 = 240 \times 10^6$, while in the first case it is 20×10^6. In further cases of individual trajectories we take $t = 12 \times 10^6$, so that the total numbers of points in both cases are equal.

Following the same method as in the two-qubit system, we can study the similarity of the patterns of the color plots by using the Frobenius distance [46]:

$$D(A, B) = \sqrt{\sum_{i,j,k} |A_{ijk} - B_{ijk}|^2}, \qquad (17)$$

where A and B are the 3D arrays which contain the counts inside the bins of two color plots. We note here that we always divide the distributions represented by matrices A and B by the quantities $N_A = N_{p_A} t_A$ and $N_B = N_{p_B} t_B$, where N_{p_A} and N_{p_B} are the number of particles in A and B, and t_A and t_B are the corresponding time of the measurement of A and B. This reduction guarantees the correct comparison of the arrays, given the fact that the sampling time Δt is common for all trajectories.

A first application of the Frobenius distance D is in checking the approach of the long time pattern of the points of individual trajectories, by comparing the patterns from $t = 5 \times 10^5$ up to $t = 1.2 \times 10^7$ [Fig. 5(a)] for different amounts
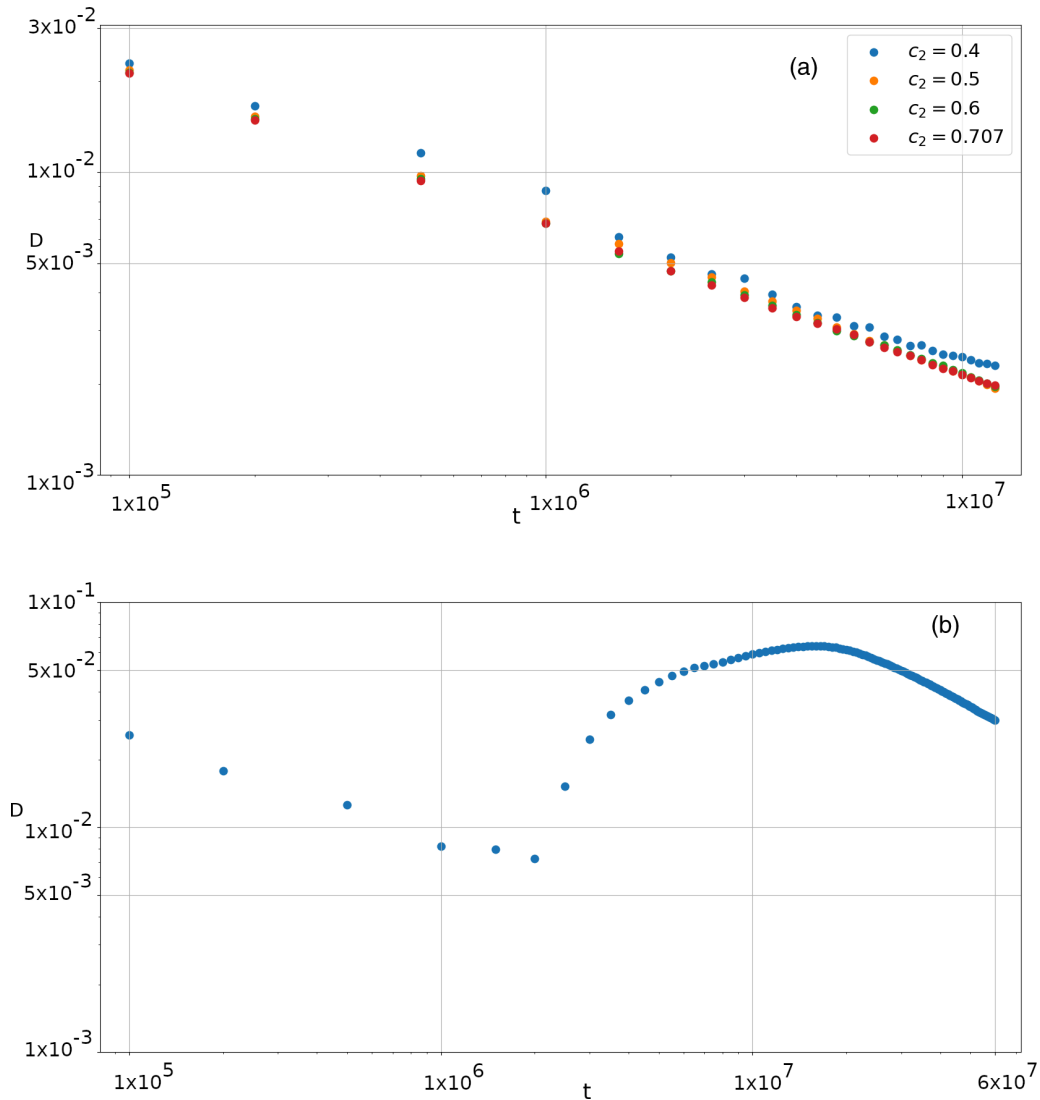
FIG. 6. The Frobenius distances between the patterns of the points of two trajectories with the same c_2 as functions of the time (a) for $c_2 = 0.4, 0.5, 0.6$, and 0.707 up to time $t = 1.2 \times 10^7$. In all cases the long limit variations of D follow a straight line in log-log scale with inclination $\simeq -0.49$ and (b) for $c_2 = 0.3$ up to $t = 6 \times 10^7$. In this case there is a large increase of D beyond $t \simeq 2 \times 10^6$ but in the long run D decreases linearly in time, in log-log scale, with an inclination roughly equal to -0.7.

of entanglement. We find that all these Frobenius distances decrease for large t and tend to zero. The distances of the cases with $c_2 \geqslant 0.4$ (strongly entangled states) decrease monotonically in time and reach values smaller than $D = 0.0001$ beyond $t = 10^7$. In the cases $c_2 = 0.1, 0.2$, and 0.3 (weakly entangled states) we have some considerable increases after $t = 25 \times 10^5$ and then decreases, but their values are still between 0.005 and 0.01 at 1.2×10^7. On the other hand, in the case of 2400 particles satisfying Born's rule for $t = 100, 200, 300, \ldots, 5000$ in Fig. 5(b), the Frobenius distances decrease very fast and become smaller than $D = 0.0002$ for $t = 5000$. For longer times this number D decreases even further and tends to zero.

Then we calculated the Frobenius distance between the patterns of the points of two chaotic trajectories in the cases $c_2 = \sqrt{2}/2, 0.6, 0.5$, and 0.4 (strong entanglement regime) up to time $t = 1.2 \times 10^7$. We found that it decreases mono-

tonically in time and becomes smaller than $D = 0.002$ for $t > 1.2 \times 10^7$ [Fig. 6(a)].

However, the corresponding distance in the weakly entangled case $c_2 = 0.3$ decreases up to time $t \simeq 4 \times 10^6$ but then increases up to a maximum $D = 0.64$ at $t \simeq 1.6 \times 10^7$ [Fig. 6(b)]. Finally it decreases monotonically and reaches a value $D = 0.03$ after $t = 6 \times 10^7$. From Fig. 6(b) we estimate by a rough extrapolation that D should be smaller than $D = 0.01$ after time $t = O(1 \times 10^8)$, decreasing further towards $D = 0$.

For such long times the accurate calculation of the trajectories becomes very difficult and requires an extremely long computer time. Our computations were made with the adaptive step size solver DLSODA in PYTHON 2.7 [47] with an absolute error tolerance of 10^{-10} and a relative error tolerance of 10^{-6}. However, there were a few times when the integrator could not achieve this accuracy due to the existence
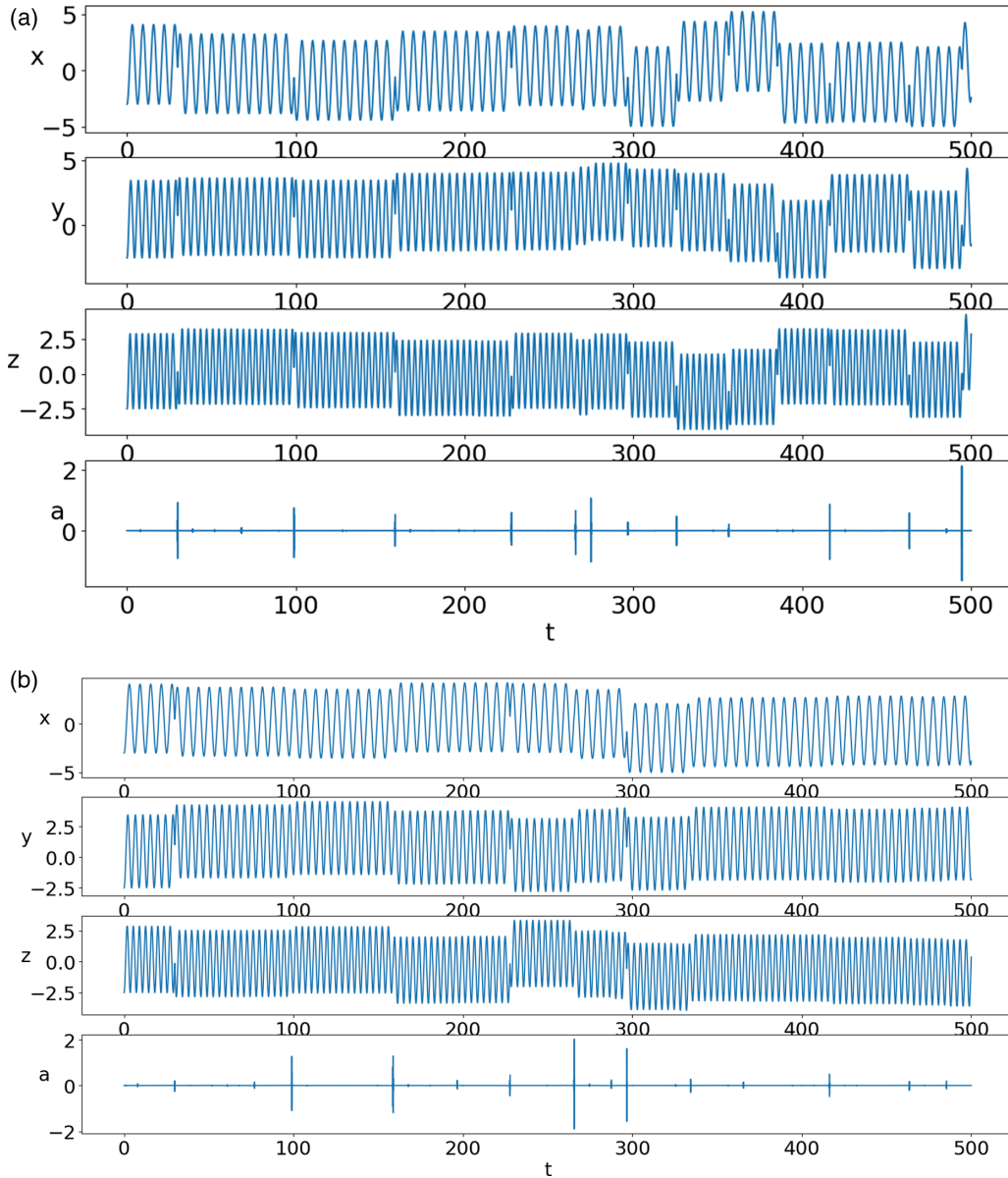
FIG. 7. The time series of x, y, and z and the corresponding stretching number of a chaotic trajectory: in the maximally entangled state with $c_2 = \sqrt{2}/2$ (a) and in the weakly entangled state with $c_2 = 0.3$ (b).

of Bohmian vortices close to the nodal points and the calculations were aborted.[5] Our conclusion is that for weakly entangled states ($c_2 \leqslant 0.3$) the chaotic trajectories are ergodic, but their ergodic character is established after extremely long times. On the other hand, the ergodicity of the chaotic trajectories of the strongly entangled states ($c_2 \geqslant 0.4$) can be established (approximately) after times smaller than $t = 10^7$.

We note that the chaotic trajectories of the present problem are not just irregular motions in 3D space but they have a certain structure. In fact the chaotic character of the trajectories

stems from their successive close encounters with the NPX-PCs. Between these approaches every trajectory tries to form a Lissajous figure. The deviation between every prescattering and postscattering Lissajous figure is larger if the approach to a NPXPC is closer and with a smaller velocity. However, there are approaches which are not very close to the NPXPCs or they occur very fast. In such cases the trajectory continues along the same Lissajous figure for more periods. This is shown in Fig. 7 where we give the functions $x(t)$, $y(t)$, and $z(t)$ for times up to $t = 500$ in the case of the maximum entanglement [panel (a)] and in the case of a chaotic trajectory when $c_2 = 0.3$ [panel (b)]. Below these functions we give the "local Lyapunov stretching number a" [48]. The scattering events correspond to the abrupt changes of a.

We further observe that up to the first collision at $t \simeq 30$, we have almost periodic motions with frequencies $\omega_x = 1$,

---

[5]The comparison of two trajectories for time $t = 6 \times 10^7$ took about 6 h in the high-performance computer of RCAAM which has 20 cpu threads and 128 GB of RAM. Similar (or longer) times are required for $c_2 = 0.2$ and $c_2 = 0.1$.
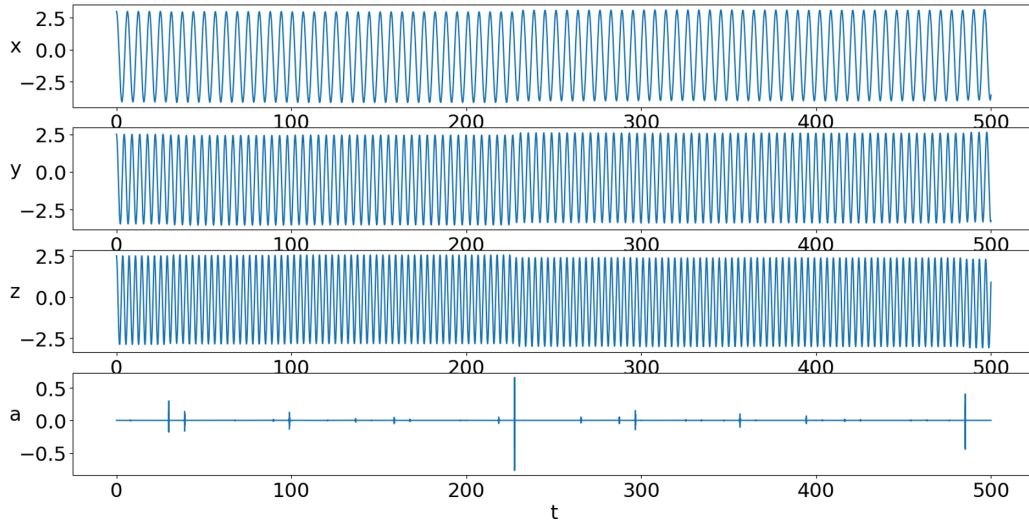
FIG. 8. The time series of x, y, and z and the corresponding stretching number of an ordered Lissajous-like trajectory in the partially entangled state with $c_2 = 0.3$.

$\omega_y = \sqrt{2}$, and $\omega_z = \sqrt{3}$. Thus there are $\frac{t}{T_x} \simeq 5$ oscillations in x, $\frac{t}{T_y} \simeq 7$ oscillations in y, and $\frac{t}{T_z} \simeq 8$ oscillations in z. The trajectories form approximately a 3D Lissajous figure of size $\Delta_x = 2x_c = 7.1$, $\Delta_y = 2y_c = 5.9$, and $\Delta_z = 2z_c = 5.4$. After various transitions the trajectory forms approximately new 3D Lissajous figures with the same frequencies and the same sizes, but with irregular positions. On the other hand, in the case of ordered trajectories the changes of the approximate Lissajous figures are very small, as in the example of Fig. 8. In fact, ordered trajectories appear mainly close to the center of the main hyperblob for small values of c_2. At the collisions between the two hyperblobs when x, y, and z are small, the nodal lines are relatively far from the center. In fact, if $|\cos(\omega_x t)|$ and $|\cos(\omega_y t)|$ are smaller than, say, 0.1, the minimum distance of a straight line from the z axis [Eq. (11)] is larger by a factor 10 from the numerical value of Eq. (12).

Furthermore the minimum value $d_{\min}$ of Eq. (12) is proportional to $\ln(|\frac{c_1}{c_2}|)$; i.e., it increases when c_2 decreases. Thus the ordered trajectories are more frequent when c_2 is smaller, as expected.

V. ORDERED AND CHAOTIC TRAJECTORIES IN THE BORN DISTRIBUTION

The ordered trajectories appear, in general, close to the center (x_c, y_c, z_c) of the leading hyperblob, while in the outer part of this hyperblob the trajectories are chaotic. Furthermore, it seems that all the trajectories of the small hyperblob are chaotic, since during the collisions of the hyperblobs the small one is fully deformed and the trajectories of its particles are all prone to scattering events (as in the corresponding two-qubit case).

The distinction between order and chaos is usually made by use of the Lyapunov characteristic number (LCN). The finite time LCN is $\chi(t) = \frac{\ln(\frac{\xi}{\xi_0})}{t}$, where ξ_0 and ξ are infinitesimal deviations at times $t_0 = 0$ and t. The limit of $\chi(t)$ when $t \to \infty$ is the LCN, namely, $LCN = \lim_{t \to \infty} \chi(t)$.

In the case of the ordered trajectories the value of $\chi(t)$ is roughly proportional to $1/t$ (in logarithmic axes) [Fig. 9(a)]; therefore, the limiting value of LCN is equal to zero. On the other hand, in the case of a chaotic trajectory $\chi(t)$ saturates at a positive value [Fig. 9(b)], and thus the LCN is positive. The
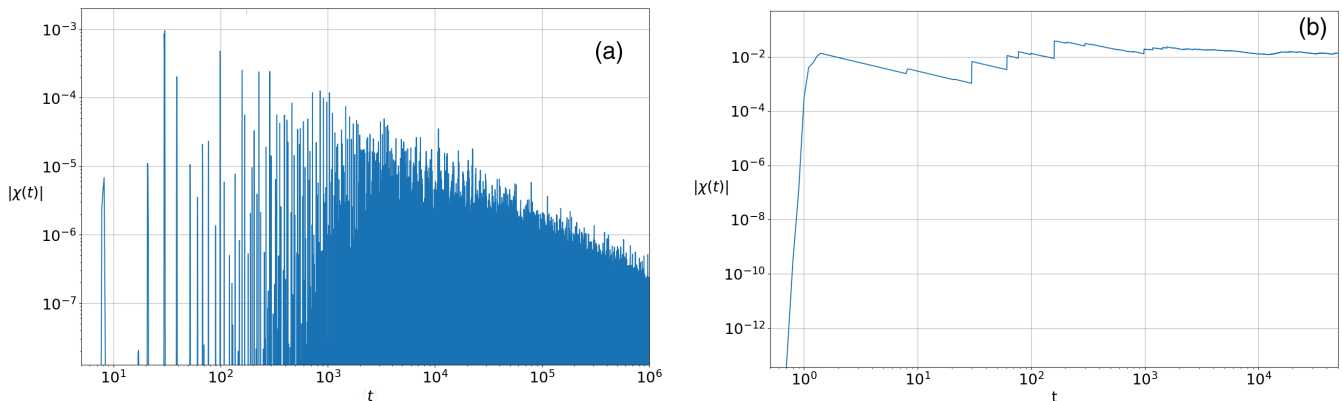
FIG. 9. The time series of the finite-time Lyapunov characteristic number in the case $c_2 = 0.2$ for (a) an ordered trajectory with $x_0 = 3.5$, $y_0 = 3.5$, and $z_0 = 2$ and (b) a chaotic trajectory with $x_0 = -3$, $y_0 = -3$, and $z_0 = -3$.
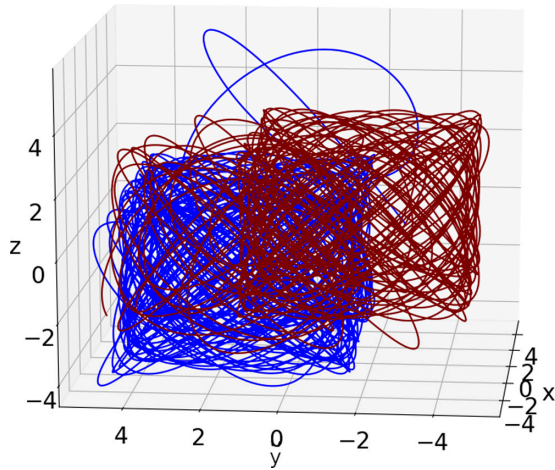
FIG. 10. Two temporary 3D Lissajous figures in the trajectory of a weakly entangled state with $c_2 = 0.1$ and $x_0 = -2$, $y_0 = -3$, and $z_0 = 0.5$ up to $t = 600$. The blue curve is closer to the observer than the red one. The trajectory forms the blue curve up to $t \simeq 320$ and then, after a scattering event, deviates and forms the red curve for the rest of the motion.

FIG. 11. The proportion of the chaotic trajectories in the Born distribution as a function of the entanglement parameter c_2 in the 2D case (red squares for $t = 10^4$) and in the 3D case (blue squares for $t = 10^5$).

temporary decreases of $\chi(t)$ correspond to time intervals in which the trajectory tends to form a Lissajous figure, while the abrupt positive shifts of $\chi(t)$ correspond to scattering events between the trajectory and the NPXPCs, which mostly occur during the collision of the hyperblobs of $|\Phi|^2$. An example of the temporary Lissajous figures is shown in Fig. 10, where we plot with different colors two successive Lissajous figures during the evolution of a trajectory in the case of $c_2 = 0.1$. The superposition of many such temporary Lissajous figures produces the final long limit pattern of the points of the chaotic trajectory.

We now proceed further to an estimation of the proportions of the chaotic and the ordered trajectories (P_{ch} and $P_{ord} = 1 - P_{ch}$) in the Born distribution, as functions of the entanglement.

Apparently, it is practically impossible to calculate all the LCNs of 2400 trajectories, due to the extremely long computational time needed for this task. Instead, we use a method that we developed in our last paper [32]. Namely, we exploit the fact that the ordered trajectories are confined in a restricted volume that is similar to the parallelepiped of the 3D Lissajous figures (Fig. 1). Therefore we can check whether a trajectory is confined inside a box, somewhat larger than a 3D Lissajous figure, or whether it goes out of this box. In the latter case the trajectory is characterized as chaotic. Although this is an approximate method, it provides reliable results, provided that the integration times are sufficiently large.

By applying this method, in Fig. 11 we make a comparison of the proportion P_{ch} of the chaotic trajectories in the Born distribution in the cases of two and three qubits (red and blue squares, correspondingly) for various degrees of entanglement. We found reliable results by taking integration times up to $t = 10^4$ (in the 2D case) and $t = 10^5$ (in the 3D case). In fact, the chaotic character of the 3D trajectories requires times to be established that are much longer than those in the 2D trajectories, because, in order to have collisions in the 3D case, we must have all three coordinates x, y, and z close to
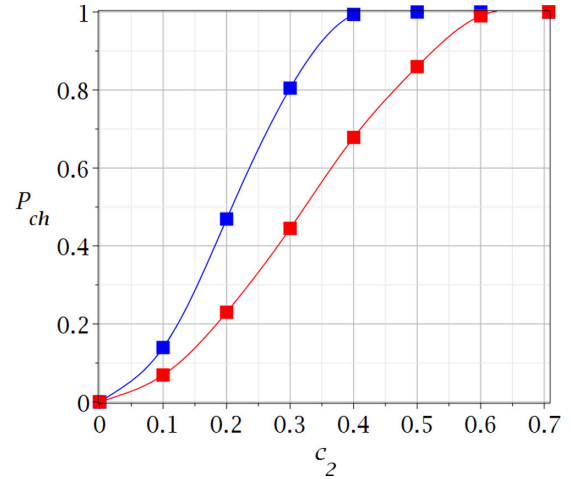
zero, while in the 2D case we require only x and y to be close to zero. We checked that larger values of integration times do not affect our results.

First we see that P_{ch} is equal to 0 for the product states and equal to 1 for the maximally entangled states in both two-qubit and three-qubit systems, as expected. Then we observe that the transition from two qubits to three qubits implies a drastic increase of P_{ch} for all partially entangled states. In fact, for every $c_2 \in (0, 0.3)$ we observe the doubling of P_{ch}, while for $c_2 \in [0.4, \sqrt{2}/2]$, practically all the 3D trajectories are chaotic. Thus in the 3D case the range of the values of the entanglement parameter for which all the trajectories are chaotic and ergodic is three times larger than in the 2D case. This is the most important difference between the two-qubit and the three-qubit system.

Further numerical evidence supporting the above results can also be found if we study the Frobenius distance between the patterns of the points of individual trajectories for various values of c_2 and various times t and the patterns of the points of 2400 trajectories satisfying Born's rule at $t = 5000$. [At this time the pattern of the BR distribution is practically finalized, as seen in Fig. 5(b)].

We see that the Frobenius distances of the cases $c_2 = 0.4$, 0.5, 0.6, and 0.707 approach well to zero with increasing time (almost linearly with an approximate inclination $\simeq -0.4$ in log-log scale). Namely, for $t = 1.2 \times 10^7$ the value of D has reached values of order $D = 0.002$ [Fig. 12(a)]. This means that, for these values of the entanglement, the patterns are not only close to each other, as we have seen in Fig. 6(a), but they also approach the patterns of the corresponding Born's rule distribution. However, for $c_2 = 0.3$ the distance between the patterns of individual trajectories increases considerably beyond $t = 0.6 \times 10^7$ and tends to be stabilized beyond $t = 6 \times 10^7$ at a value close to $D = 0.1$ [Fig. 12(b)]. This value is much larger than that of the distance between individual chaotic trajectories for the same amount of entanglement and the same time [Fig. 6(b)]. We have seen that this distance between two chaotic trajectories decreases and tends to zero for
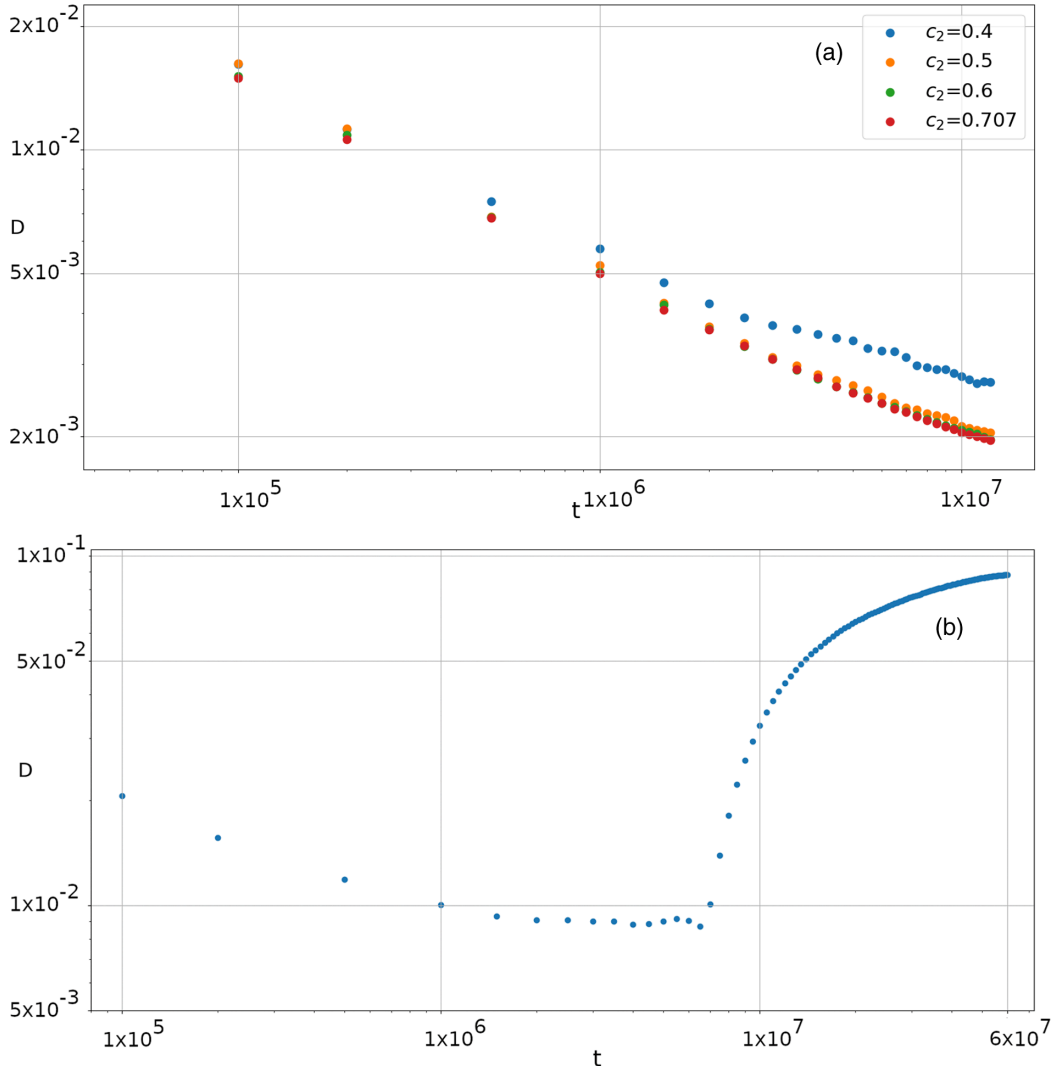
FIG. 12. The Frobenius distance between the patterns of a single chaotic trajectory at various times compared with the corresponding pattern of the Born distribution of 2400 particles at $t = 5000$ (a) for $c_2 = 0.4, 0.5, 0.6$, and 0.707 up to time $t = 1.2 \times 10^7$ and (b) for $c_2 = 0.3$ up to time $t = 6 \times 10^7$.

much larger times, while the distance from the BR distribution remains large [Fig. 12(b)].

Similar results were found for $c_2 = 0.2$ and $c_2 = 0.1$. Therefore we conclude that in the 3D case considered in the present paper the chaotic trajectories are also ergodic, for every $c_2 \neq 0$. But, while for $c_2 \geqslant 0.4$ these trajectories form patterns approaching closely the patterns of the corresponding Born distributions, the chaotic trajectories for $c_2 \leqslant 0.3$ form ergodic patterns that are distinctly different from the corresponding BR patterns. However, this difference appears after a very long time, because, for given time t, the collisions of the two hyperblobs in the 3D case are much less frequent than in the 2D case.

Taking all the above considerations into account, it is natural to expect that a similar increase of the chaotic trajectories will appear in more dimensions (N-qubit systems with $N > 3$). Thus we conjecture that for $N > 5$ the vast majority of the 3D trajectories are chaotic and Born's rule will be accessible by most initial distributions of particles.

VI. CONCLUSIONS

In this work we studied the ordered and chaotic Bohmian trajectories of a three-qubit system, composed of coherent states of the quantum harmonic oscillator in x, y, and z directions, and their role in the dynamical establishment of Born's rule.

Many results of our study are analogous to those of the two-qubit system.

(i) We have considered a two-qubit wave function $\Phi = c_1 Y_R(x, t) Y_R(y, t) Y_R(z, t) + c_2 Y_L(x, t) Y_L(y, t) Y_L(z, t)$ and calculated its probability density $|\Phi|^2$, for various values of the entanglement. In close analogy to the 2D case, the function $|\Phi|^2$ consists of two hyperblobs which are equal if $c_1 = c_2$ and only one hyperblob in the product states $c_2 = 0$ and $c_1 = 0$. For $c_1 \cdot c_2 \neq 0$ the two hyperblobs are located very close to the single hyperblobs of the two product states, except when the hyperblobs collide.

(ii) If the two hyperblobs are populated by particles, then during the collisions some particles are exchanged between

the two hyperblobs. Exchanges appear when the particles approach a nodal line where $\Phi_{\text{real}} = \Phi_{\text{imag}} = 0$. The nodal lines are straight lines, infinite in number, that move around in time. For every value of z the nodal lines define nodal points, which are at equal distances from each other for any c_2 and z, but these distances change in time. According to the NPXPC mechanism for 3D systems, close to the nodal lines are the X-lines which scatter the incoming particles and produce chaos.

(iii) After a collision the two hyperblobs of the wave function are formed again and consist of mixtures of particles of the initial hyperblobs.

(iv) The trajectories of the particles are either chaotic or ordered. Similarly to the 2D case, the ordered trajectories appear close to the center of the major hyperblob. In the absence of entanglement we have only ordered trajectories, which are 3D Lissajous figures, while the ordered trajectories of the partially entangled states are, in general, deformed Lissajous figures.

(v) The chaotic trajectories are ergodic. Namely, the final distribution of their points does not depend on the initial conditions and consists of eight high-concentration regions near the corners of its pattern, similarly to the four high-concentration regions of the 2D case. Further away from the center, the density of points decreases and tends to zero. The final distribution is approached after a time of order $t = 10^6$ for strongly entangled states and after times of order $t = 10^8$ for weakly entangled states. These times are much larger than those in the two-qubit case, due to the increased dimensionality of the system.

(vi) For weakly entangled states, the various patterns of the long limit distributions of the points of single chaotic trajectories deviate from the corresponding patterns of the distributions satisfying BR. These deviations are due to the existence of ordered trajectories in the BR distributions. Thus, only the initial distributions with the proper ratio between chaotic and ordered trajectories will approach the BR distribution, as in the two-qubit case.

However, there is an important difference between the three-qubit and the two-qubit systems: In the 3D case there is a remarkable increase of the chaotic and ergodic trajectories for every nonzero entanglement, in comparison with the two-qubit case. This is due to the existence of significantly more NPXPCs than in the 2D case.

Our main conclusion is that by increasing the dimensionality of our system, the number of NPXPCs grows, and so does the number of chaotic trajectories. It is natural to expect that this behavior will become even more evident if we add further qubits, i.e., more degrees of freedom. As a consequence, the Born rule will be reachable, after very long times, for the majority of initial preparations in multiqubit systems.

APPENDIX

The nodal lines are found by solving the equations $\Phi_{\text{Real}} = \Phi_{\text{Imag}} = 0$. We have

$$
\left(\frac{\omega_x \omega_y \omega_z}{\pi^3}\right)^{-\frac{1}{4}} (\Phi_{\text{Real}} + i\Phi_{\text{Imag}})
$$

$$
= c_1 \exp\left[-\frac{\omega_x}{2}\left(x - \sqrt{\frac{2}{\omega_x}}a_0\cos(\omega_x t)\right)^2 - \frac{\omega_y}{2}\left(y - \sqrt{\frac{2}{\omega_y}}a_0\cos(\omega_y t)\right)^2 - \frac{\omega_z}{2}\left(z - \sqrt{\frac{2}{\omega_z}}a_0\cos(\omega_z t)\right)^2\right]
$$

$$
\times [\cos(A_x) + i\sin(A_x)][\cos(A_y + i\sin(A_y)][\cos(A_z) + i\sin(A_z)]
$$

$$
+ c_2 \exp\left[-\frac{\omega_x}{2}\left(x + \sqrt{\frac{2}{\omega_x}}a_0\cos(\omega_x t)\right)^2 - \frac{\omega_y}{2}\left(y + \sqrt{\frac{2}{\omega_y}}a_0\cos(\omega_y t)\right)^2 - \frac{\omega_z}{2}\left(z + \sqrt{\frac{2}{\omega_z}}a_0\cos(\omega_z t)\right)^2\right]
$$

$$
\times [\cos(B_x) + i\sin(B_x)][\cos(B_y) + i\sin(B_y)][\cos(B_z) + i\sin(B_z)] = 0, \tag{A1}
$$

where

$$
A_x = -\sqrt{2\omega_x}a_0 x \sin(\omega_x t) + \frac{a_0^2 \sin(2\omega_x t) - \omega_x t}{2}
$$

$$
B_x = \sqrt{2\omega_x}a_0 x \sin(\omega_x t) + \frac{a_0^2 \sin(2\omega_x t) - \omega_x t}{2}. \tag{A2}
$$

The expressions of A_y, B_y, A_z, and B_z are similar to A_x and B_x. We only replace x by y (or z) and ω_x by ω_y (or ω_z). From Eq. [12] we find the following by dividing by c_2 and by the exponential of c_2:

$$\frac{c_1}{c_2} \exp \Omega \{\cos(A_x + A_y + A_z) + \cos(B_x + B_y + B_z)\} = 0,$$

$$\frac{c_1}{c_2} \exp \Omega \{\sin(A_x + A_y + A_z) + \sin(B_x + B_y + B_z)\} = 0, \tag{A3}$$

where $\Omega = 2a_0[\sqrt{2\omega_x}x\cos(\omega_x t) + \sqrt{2\omega_y}y\cos(\omega_y t) + \sqrt{2\omega_z}z\cos(\omega_z t)]$. From these equations we derive $\sin(A_x + A_y + A_z - B_x - B_y - B_z) = 0$, and hence $A_x + A_y + A_z - B_x - B_y - B_z = k\pi$, $k \in Z$. Consequently

$$\sqrt{2\omega_y}a_0 y = \left(\frac{k\pi}{2} - \sqrt{2\omega_x}a_0 x \sin(\omega_x t) + \sqrt{2\omega_z}a_0 z \sin(\omega_z t)\right) / \sin(\omega_y t). \tag{A4}$$

Then from Eqs. (A3) we derive

$$\frac{c_1}{c_2} \exp(\Omega) = -\frac{\cos(B_x + B_y + B_z)}{\cos(A_x + A_y + A_z)} = -\frac{\sin(B_x + B_y + B_z)}{\sin(A_x + A_y + A_z)} = \pm 1. \tag{A5}$$

This is 1 if k is odd and then $c_1 \cdot c_2 > 0$, or it is -1 if k is zero or even, and then $c_1 \cdot c_2 < 0$. Furthermore, by use of Eq. (A4) we find

$$\Omega = \frac{k\pi \cos(\omega_y t) - 2\sqrt{2\omega_x}a_0 x \sin(\omega_{xy}t) - 2\sqrt{2\omega_z}a_0 z \sin(\omega_{zy}t)}{\sin(\omega_y t)}. \tag{A6}$$

Then, taking the logarithms in Eq. (A5) we find

$$\ln\left(\left|\frac{c_1}{c_2}\right|\right) + [k\pi \cos(\omega_y t) - 2\sqrt{2\omega_x}a_0 x \sin(\omega_{xy}t) - 2\sqrt{2\omega_z}a_0 z \sin(\omega_{zy}t)]/\sin(\omega_y t) = 0. \tag{A7}$$

Therefore, by using also Eq. (A4), we find

$$x_{\text{nod}} = \frac{k\pi \cos(\omega_y t) + \sin(\omega_y t)\ln\left(\left|\frac{c_1}{c_2}\right|\right) - 2\sqrt{2\omega_z}a_0 z \sin(\omega_{zy}t)}{2\sqrt{2\omega_x}a_0 \sin(\omega_{xy}t)}, \tag{A8}$$

$$y_{\text{nod}} = -\frac{k\pi \cos(\omega_x t) + \sin(\omega_x t)\ln\left(\left|\frac{c_1}{c_2}\right|\right) - 2\sqrt{2\omega_z}a_0 z \sin(\omega_{zx}t)}{2\sqrt{2\omega_y}a_0 \sin(\omega_{xy}t)}. \tag{A9}$$

[1] D. Bohm, Phys. Rev. **85**, 166 (1952).
[2] D. Bohm, Phys. Rev. **85**, 180 (1952).
[3] D. Dürr and S. Teufel, *Bohmian Mechanics* (Springer, Berlin, 2009).
[4] L. De Broglie, C. R. Acad. Sci., Paris **183**, 447 (1926).
[5] L. de Broglie, Nature (London) **118**, 441 (1926).
[6] L. De Broglie, C. R. Acad. Sci., Paris **184**, 273 (1927).
[7] L. De Broglie, C. R. Acad. Sci., Paris **185**, 380 (1927).
[8] D. Bohm and J.-P. Vigier, Phys. Rev. **96**, 208 (1954).
[9] A. Valentini, Phys. Lett. A **156**, 5 (1991).
[10] A. Valentini, Phys. Lett. A **158**, 1 (1991).
[11] D. Dürr, S. Goldstein, and N. Zanghi, J. Stat. Phys. **67**, 843 (1992).
[12] A. Valentini and H. Westman, Proc. R. Soc. A **461**, 253 (2005).
[13] M. Towler, N. Russell, and A. Valentini, Proc. R. Soc. A **468**, 990 (2011).
[14] E. Abraham, S. Colin, and A. Valentini, J. Phys. A **47**, 395306 (2014).
[15] S. Colin and A. Valentini, Proc. R. Soc. A **470**, 20140288 (2014).
[16] N. G. Underwood, J. Phys. A **51**, 055301 (2017).
[17] D. Dürr and W. Struyve, *Do Wave Functions Jump?* edited by V. Allori, A. Bassi, D. Dürr, and N. Zanghi (Springer, Berlin, 2020), p. 35.
[18] H. Frisk, Phys. Lett. A **227**, 139 (1997).

[19] I. Bialynicki-Birula, Z. Bialynicka-Birula, and C. Śliwa, Phys. Rev. A **61**, 032110 (2000).
[20] P. Falsaperla and G. Fonte, Phys. Lett. A **316**, 382 (2003).
[21] A. S. Sanz, F. Borondo, and S. Miret-Artés, Phys. Rev. B **69**, 115413 (2004).
[22] D. A. Wisniacki and E. R. Pujals, Europhys. Lett. **71**, 159 (2005).
[23] D. A. Wisniacki, E. R. Pujals, and F. Borondo, Europhys. Lett. **73**, 671 (2006).
[24] D. Wisniacki, E. Pujals, and F. Borondo, J. Phys. A **40**, 14353 (2007).
[25] F. Borondo, A. Luque, J. Villanueva, and D. A. Wisniacki, J. Phys. A **42**, 495103 (2009).
[26] C. Efthymiopoulos and G. Contopoulos, J. Phys. A **39**, 1819 (2006).
[27] C. Efthymiopoulos, C. Kalapotharakos, and G. Contopoulos, Phys. Rev. E **79**, 036203 (2009).
[28] A. C. Tzemos, C. Efthymiopoulos, and G. Contopoulos, Phys. Rev. E **97**, 042201 (2018).
[29] A. C. Tzemos, G. Contopoulos, and C. Efthymiopoulos, Phys. Scr. **94**, 105218 (2019).
[30] A. C. Tzemos and G. Contopoulos, Phys. Scr. **95**, 065225 (2020).
[31] A. C. Tzemos and G. Contopoulos, Phys. Rev. E **102**, 042205 (2020).

[32] A. Tzemos and G. Contopoulos, Phys. Scr. **96**, 065209 (2021).

[33] M. A. Nielsen and I. L. Chuang, *Quantum Computation and Quantum Information* (Cambridge University, Cambridge, England, 2004).

[34] J. Asbóth, P. Adam, M. Koniorczyk, and J. Janszky, Eur. Phys. J. D **30**, 403 (2004).

[35] J. Garrison and R. Chiao, *Quantum Optics* (Oxford University Press, Oxford, 2008).

[36] S. Goldstein, Found. Phys. **40**, 335 (2010).

[37] M.-J. Yang and S.-T. Wu, Phys. Rev. A **89**, 022301 (2014).

[38] R. Horodecki, P. Horodecki, M. Horodecki, and K. Horodecki, Rev. Mod. Phys. **81**, 865 (2009).

[39] C. Zander and A. Plastino, Entropy **20**, 473 (2018).

[40] T. A. Elsayed, K. Mølmer, and L. B. Madsen, Sci. Rep. **8**, 12704 (2018).

[41] Y. Aharonov, N. Erez, and M. O. Scully, Phys. Scr. **69**, 81 (2004).

[42] F. Avanzini and G. J. Moro, J. Phys. Chem. A **121**, 5352 (2017).

[43] A. C. Tzemos, G. Contopoulos, and C. Efthymiopoulos, Phys. Lett. A **380**, 3796 (2016).

[44] G. Contopoulos, A. C. Tzemos, and C. Efthymiopoulos, J. Phys. A **50**, 195101 (2017).

[45] S. Szalay, Phys. Rev. A **92**, 042329 (2015).

[46] G. Strang, *Introduction to Linear Algebra* (Wellesley-Cambridge, Wellesley, MA, 1993).

[47] S. Linge and H. P. Langtangen, *Programming for Computations-Python: A Gentle Introduction to Numerical Simulations with Python* (Springer, Cham, 2016).

[48] G. Contopoulos, *Order and Chaos in Dynamical Astronomy* (Springer, Berlin, 2002).